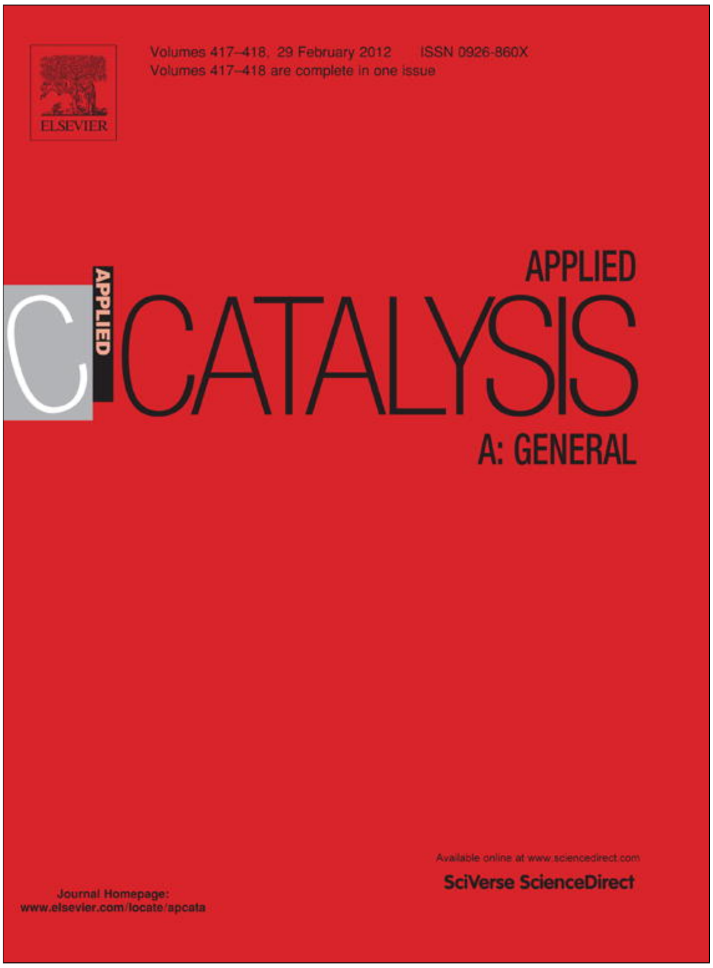

Volumes 417–418, 29 February 2012 ISSN 0926-860X
Volumes 417–418 are complete in one issue

APPLIED
CATALYSIS
A: GENERAL

Available online at www.sciencedirect.com
SciVerse ScienceDirect

Journal Homepage:
www.elsevier.com/locate/apcata

Applied Catalysis A: General 417–418 (2012) 43–52

Contents lists available at SciVerse ScienceDirect

Applied Catalysis A: General

journal homepage: www.elsevier.com/locate/apcata

Application of ETS-10 microporous titanosilicate as support of Ru nanoparticles for hydrogen production

B.M. Faroldi [a], E.A. Lombardo [a], L.M. Cornaglia [a,*], S. Irusta [b]

[a] *Instituto de Investigaciones en Catálisis y Petroquímica (FIQ, UNL-CONICET), Santiago del Estero, 2829-3000 Santa Fe, Argentina*
[b] *Instituto de Nanociencia de Aragón (INA), Universidad de Zaragoza, Mariano Esquillor s/n (50018), Zaragoza, Spain*

ARTICLE INFO

Article history:
Received 15 October 2011
Received in revised form
12 December 2011
Accepted 13 December 2011
Available online 22 December 2011

Keywords:
Ruthenium
ETS-10
Dry reforming
Hydrogen production

ABSTRACT

Supported ruthenium catalysts have been shown to be effective for the dry reforming of methane. Besides, ETS-10 titanosilicate has properties able to disperse Ru species. In this work, microporous ETS-10 titanosilicate was synthesized by hydrothermal synthesis employing anatase as Ti source. Ru was incorporated using three different methods: by incipient wetness impregnation (RuH), by ion exchange (RuI) and by adding Ru to the gel synthesis (RuG). The species present in the solids were characterized by XRD, N_2 adsorption, ICP, SEM, TEM, EDX, TGA, TPR, UV–vis and XPS.

RuH and RuI catalysts were found to be active and stable for the dry reforming of methane. These results show the potential application of ETS-10 as support of Ru catalysts for the production of hydrogen.

1. Introduction

The simultaneous incorporation of octahedral Ti $[TiO_6]^{2-}$ and tetrahedral Si $[SiO_4]$ microporous materials has led to the appearance of a new family of microporous crystalline titanosilicates, materials mainly inspired in similar compounds found in nature, which has generated great interest from the viewpoint of catalytic processes and ion exchange. ETS-10 (Engelhard titanosilicate Structure 10), one of the main members in the family of titanosilicates, presents a structure similar to that of inorganic microporous zeolites [1]. In fact, the topological similarities between ETS-10 and β zeolite (aluminosilicate three-dimensional channels with micropores of 0.71 nm × 0.73 nm) are remarkable. Titanosilicate Ti atoms are octahedrally connected to four Si and two Ti atoms through oxygen bonds, giving rise to a three-dimensional structure with a significant degree of disorder [2]. The disordered material can be described by two ordered polymorphs, arranged in layers. The porous structure consisting of rings of 12, 7, 5 and 3 members has a three-dimensional pore system whose minimum diameter is defined by the 12-member rings, with a micropore size of 0.49 nm × 0.76 nm. A network of tetrahedral SiO_4 and octahedral TiO_6 is associated with a charge of −2 compensated by cations mainly located in areas adjacent to the Ti chains and 12- and 7-member rings. The stoichiometry of ETS-10 is given by $M_2TiSi_5O_{13}\cdot 4H_2O$ where M: Na^+ and K^+ are compensation cations. Cation density is high, roughly equivalent to that of a zeolite with a Si/Al = 2.5, for example Y zeolite.

This titanosilicate has some advantages over other similar materials, such as the possibility of synthesis based on different sources of Ti and the presence of a pure phase which can be obtained in the absence of a structuring agent. Additionally, by functionalizing its structure, it is possible to modify its catalytic properties and adsorption isomorphic substitution, or its high ion exchange capacity, hydrophilicity and basicity.

Few studies have employed ETS-10 as catalyst support. However, some encouraging results are related to the activity and selectivity of the titanosilicate. Anderson and coworkers [3] have synthesized Pt/ETS-10 for n-hexane reforming reporting that these solids exhibit very high selectivity. In addition, Santamaría and coworkers [4] have used Pt/ETS-10 catalysts for the selective oxidation of CO in the presence of H_2, CO_2 and H_2O.

Bueno and co-workers [5] used similar materials (NaY and mordenite) as supports for ruthenium catalysts for the dry reforming reaction. These authors reported a H_2/CO ratio close to 1, indicating that the RWGS reaction was minimized. The dry reforming of methane is important from the environmental viewpoint since these two gases contribute to the green-house effect. In addition, the use of synthesis gas as feedstock for fuel cells and for the Fischer–Tropsch reaction has brought about an increasing interest in methane reforming reactions. One of the main problems for the preparation of effective reforming catalysts is the deactivation

---

* Corresponding author. Tel.: +54 342 4536861; fax: +54 342 4536861.
E-mail addresses: lmcornag@fiq.unl.edu.ar, lmcornag@fiqus.unl.edu (L.M. Cornaglia).

0926-860X/$ – see front matter © 2011 Elsevier B.V. All rights reserved.
doi:10.1016/j.apcata.2011.12.023

due to coke formation. In the presence of noble metals and an adequate support, coke formation can be attenuated [6,7]. Dispersing the active metal on a high surface area solid and using the right promoters could improve the catalyst activity and stability.

The purpose of this study is to develop active Ru catalysts supported on ETS-10 with high resistance to carbon deposition for the dry reforming of methane at moderate temperatures (550 °C). The hydrothermal synthesis of titanosilicate ETS-10 was carried out and Ru catalysts were obtained by different preparation methods. The catalysts and supports were characterized using XRD, N_2 adsorption, ICP, SEM, TEM, EDX, TGA, TPR, UV–vis and XPS.

2. Experimental

2.1. Catalyst preparation

2.1.1. Synthesis of K/Na ETS-10 from anatase

The support was prepared according to the procedure used by Anderson et al. [8]. To prepare a gel with composition 4.4 Na_2O/1.4 K_2O/TiO_2/5.5 SiO_2/125 H_2O, the following reactants were used: sodium silicate solution (25.5–28.5% SiO_2, 7.5–8.5% Na_2O) (Merck), anatase 99.9% (Aldrich) as a source of Ti, NaCl (Carlo Erba), KCl (Riedel de Haen) and KF (Aldrich). The gel was introduced into an autoclave and was subjected to different synthesis times: 6, 12, 24 and 48 h. Then the solid was filtered and washed until the washing water reached a pH between 9 and 10. Subsequently, the solid was dried at 100 °C in an oven for 12 h.

Three strategies were followed to incorporate the ruthenium into the solid with 24 h synthesis time. In all the synthesis, $RuCl_3 \cdot 3H_2O$ was used as precursor compound.

(a) *Synthesis of cation impregnated ETS-10 (RuH).* $RuCl_3$ was impregnated by incipient wetness on the ETS-10 support and then dried at 90 °C overnight.
(b) *Synthesis of cation exchanged ETS-10 (RuI).* Ruthenium cations were exchanged into the sodium/potassium form of ETS-10 by the conventional cation exchange method from aqueous solution. Typically, ETS-10 was treated with 0.0015 M (diluted solution – RuI-DS) or 0.005 M (concentrated solution – RuI-CS) aqueous solution of ruthenium chloride with a solid/liquid ratio of 1:80 at 80 °C for 21 h and with a pH equal to 5.2. The residue was filtered, washed with hot distilled water, until the washings were free from chloride ions and dried at 90 °C in an oven overnight. The extent of ruthenium exchange on ETS-10 was determined by Inductively Coupled Plasma (ICP) and Energy dispersive X-ray (EDX) analyses.
(c) *Synthesis of cation in situ load. ETS-10 (RuG).* Ruthenium ETS-10 samples were prepared by adding $RuCl_3$ salt in situ during the gel preparation for the ETS-10 synthesis. The gel was obtained in the same way as described above and as the last step $RuCl_3$ was added, followed by stirring the slurry for 60 min at room temperature. The slurry was then transferred into a Teflon-lined autoclave, which in turn was heated statically at 230 °C for 24 h in an oven. The in situ load ETS-10 obtained was then washed with distilled water and dried at room temperature and then at 90 °C in an oven.

2.2. Supports and catalysts characterization

2.2.1. Surface area

N_2 adsorption–desorption isotherms, pore size distribution and BET area were measured at −196 °C using a Micromeritics ASAP 2020 instrument V1. Prior to the measurements, all samples were outgassed at 0.13 Pa and 200 °C during 8 h. The microporous volumen was calculated using the t-plot method.

2.2.2. X-ray diffraction (XRD)

The XRD measurements were performed at room temperature using a "D-Max Rigaku" equipped with a rotating anode. The diffractometer was operated at 40 kV and 80 mA with a Cu anode and a graphite monochromator was used to select the CuKα1,2 radiation. Measurement conditions were: 2θ: 5–60°, step = 0.03°, t = 1 s/step.

2.2.3. Metal dispersion

The metal dispersion of the fresh catalyst, following the in situ hydrogen reduction at 550 °C for 1 h, was determined by static equilibrium adsorption of CO at 25 °C in a conventional vacuum system.

2.2.4. Temperature-programmed reduction (TPR)

An Ohkura TP-20022S instrument equipped with a TCD was used for the TPR experiments. The samples were pretreated in situ in N_2 flow at 300 °C for 1 h to dehydrate the samples. Afterwards, they were reduced in a 5% H_2–Ar stream, with a heating rate of 10 °C/min up to the maximum treatment temperature.

2.2.5. X-ray photoelectron spectroscopy (XPS)

The XPS measurements were carried out using a multitechnique system (SPECS) equipped with a dual Mg/Al X-ray source and a hemispherical PHOIBOS 150 analyzer operating in the fixed analyzer transmission (FAT) mode. The spectra were obtained with a pass energy of 30 eV; an Mg-Kα X-ray source was operated at 200 W and 12 kV. The working pressure in the analyzing chamber was less than 5.9×10^{-7} Pa. The XPS analyses were performed on the supports and on the solids after treatment with hydrogen at 400 °C in the reaction chamber of the spectrometer. The spectral regions corresponding to O 1s, Si 2p, Ti 2p, Na 1s, K 2p, C1s, Ru 3d and Ru 3p core levels were recorded for each sample.

The data treatment was performed with the Casa XPS program (Casa Software Ltd, UK). The peak areas were determined by integration employing a Shirley-type background. Peaks were considered to be a mixture of Gaussian and Lorentzian functions in a 70/30 ratio. For the quantification of the elements, sensitivity factors provided by the manufacturer were used.

2.2.6. Diffuse reflectance UV–vis

The spectra of UV–vis were recorded on a Jasco V 670 equipped with a diffuse reflectance attachment with a scan rate of 200 nm/min in the range of 200–600 nm. Barium sulfate was used as white standard.

2.2.7. Thermogravimetric analyses (TGA)

The TGA experiments were performed in a TGA/SDTA851 (Mettler Toledo) instrument with a heating rate of 10 °C/min.

2.2.8. Scanning electron microscopy (SEM)

The morphology and particle sizes were studied with a SEM instrument (Hitachi S2300). In addition, samples were examined by SEM in a JEOL JSM-6400 instrument operating at 3–20 kV, which was used to perform the energy dispersive X-ray spectroscopy (EDX) analysis.

2.2.9. Transmission electron microscopy (TEM)

TEM specimens were prepared after dispersion in deionized water before pouring onto the carbon grid. TEM measurements were performed in a TEM 200: Tecnai T20, FEI and a HR Tecnai F30, FEI.

2.2.10. *Inductively coupled plasma (ICP)*

Volumetric chemical analyses were performed using the inductively coupled plasma technique with a Perkin Elmer P-40 instrument.

2.3. *Catalytic test*

The activity and stability for the dry reforming of methane of the Ru catalysts (20 mg) were evaluated in a tubular quartz reactor (inner diameter, 5 mm) which was placed into an electric oven. A thermocouple in a quartz sleeve was placed on top of the catalyst bed. The un-calcined catalysts were heated up to 550 °C in Ar flow and then reduced in H_2 flow at the same temperature for 2 h. After reduction, the reactant gas mixture ($P_{CO_2} : P_{CH_4} : P_{Ar} = 1 : 1 : 1.2$, $P = 1$ atm, $W/F = 4.5 \times 10^{-6}$ g h ml^{-1}) was fed to the reactor. The reaction experiments were carried out at 550 °C.

The reaction rate measurements under differential conditions were conducted in a conventional flow system. The gas mixture composition was analyzed by gas chromatography with a thermal conductivity detector.

In order to check the differential conditions, the forward reaction rates (r_f) were calculated from the net rate of reaction (r_n). The r_f can be estimated as follows:

$$r_f = r_n(1 - \eta)$$
$$r_n = \frac{F_{AO} X_A}{W}$$
$$\eta = \frac{(P_{CO})^2 (P_{H_2})^2}{P_{CH_4} P_{CO_2}} \frac{1}{Ke}$$

where F_{AO} is the feed molar flux of A species, X_A is the conversion of A species, W is the catalyst mass, $P_i s$ are the prevalent pressures of reactants and products and Ke is the equilibrium constant calculated at the corresponding reaction temperature. The calculated η values were lower than 1×10^{-20} confirming the quality of the differential data obtained.

3. Results and discussion

3.1. *Characterization of supports*

The ETS-10 molecular sieve is made up of a combination of tetrahedral silica and octahedral titanium units, with intersecting tubular pores with a maximum aperture of 8 Å. ETS-10 titanosilicates using TiO_2 as a source of Ti were prepared at 230 °C with different synthesis times. The presence of highly crystalline ETS-10 titanosilicate was observed in the XRD patterns of all samples (Fig. 1). The reflexion at 25.2° showed the presence of remaining TiO_2, this peak decreased with increasing synthesis time. Besides, ETS-4 as an impurity was detected for the samples with 24 and 48 h synthesis time. The appearance of this impurity with increasing synthesis time has been reported by other authors [9].

The specific surface area and specific pore volume of the synthesized materials were calculated from adsorption–desorption of N_2 data. As shown in Table 1, with increasing synthesis time the specific surface area and the pore volume of the solids also increased. The specific surface area values of ETS-10 samples which can be found in the literature vary between 230 and 460 m^2 g^{-1} [10–14]. Our solids reached the maximum of surface area (266 m^2 g^{-1}) and pore volume for a synthesis time of 24 h, when the time was increased to 48 h the surface area decreased to 229 m^2 g^{-1}.

Fig. 2 shows a SEM micrograph of one of the synthesized solids, with the typical crystal morphology of truncated bipyramid, similar to that of previous studies using different titanium sources [1,8,15]. The particle sizes for the 6, 12 and 24 h synthesis time were in the 400–500 nm range. However, for 48 h the particles sizes were

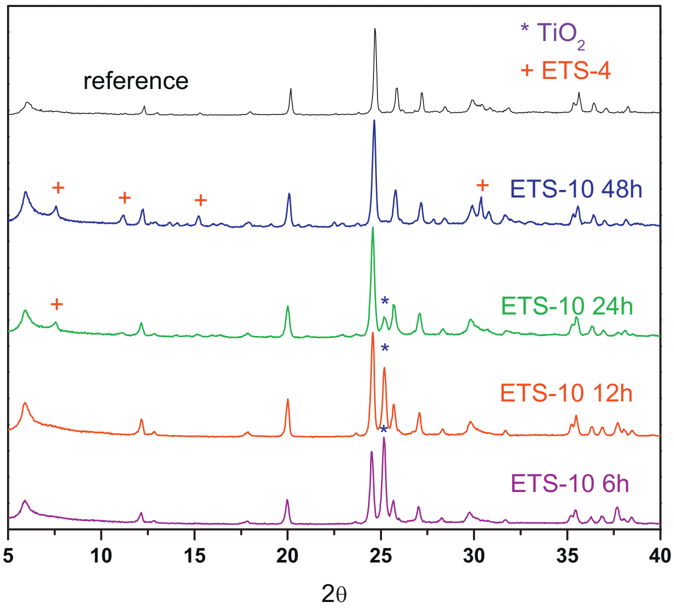

Fig. 1. XRD patterns of ETS-10 obtained at different synthesis times (6–48 h).

Table 1
ETS-10 and Ru/ETS-10 BET surface area, micropores volume and Si/Ti atomic ratio measured by ICP and EDX.

Solids	BET surface area (m^2 g^{-1})	Micropores volumen (cm^3/g)	Si/Ti ICP	Si/Ti EDX
ETS-10 6 h	174	0.07	1.9	1.7
ETS-10 12 h	187	0.08	2.7	3.7
ETS-10 24 h	266	0.12	4.1	4.6
ETS-10 48 h	229	0.10	4.5	4.8
RuH[a]	225	0.10	4.0	–
RuG[b]	305	0.13	4.4	–
RuI-DS[c]	247	0.10	3.9	–
RuI-CS[d]	267	0.11	4.2	–

[a] Ru impregnated ETS-10 24 h.
[b] $RuCl_3$ added during gel preparation.
[c] Ru exchanged (dilute solution, 0.0015 M).
[d] Ru exchanged (concentrate solution, 0.005 M).

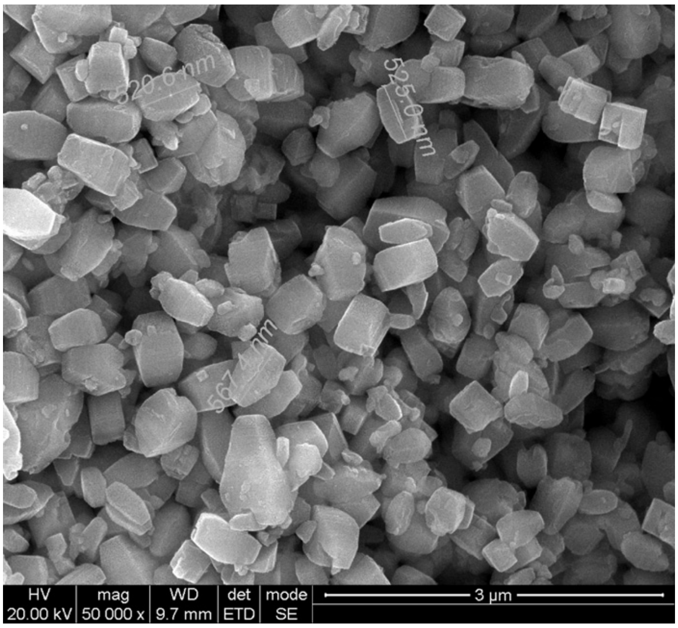

Fig. 2. SEM micrograph of crystalline materials of ETS-10-24 h.

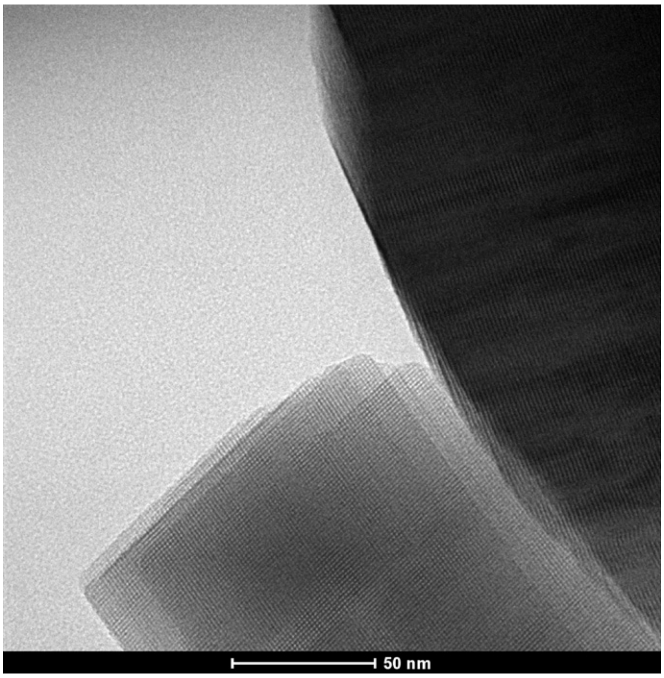

Fig. 3. TEM micrograph of ETS-10-24 h.

around 600 nm. A better detail of the crystals can be obtained from transmission electron microscopy analysis (Fig. 3). This technique allows appreciating the single crystal nature of individual ETS-10, even of nanometer size crystals [9,16]. Since the particles fell randomly on the carbon net during the TEM sample preparation, two faces of the crystals were chosen for observation. At the top right, a crystal particle with its c axis parallel to the plane of the image can be observed (Fig. 3) while at the bottom, a particle with its c axis oriented perpendicular to the plane of the picture (c plane) can also be seen. In this particle, the well-defined pattern of ETS-10 is clearly seen (Fig. 3), even the double-pore defects that seem to be created by the linking together of two channels during growth are observed [17,18]. On the other hand, 12-ring pores (0.49 nm x 0.76 nm) run parallel to the [1 0 0] and [0 1 0] directions in the ETS-10 structure, so that the straight lines clearly observed in Fig. 3, taken perpendicularly to the [0 0 1] direction, may correspond to these channels. From this figure, the distance between channels can be approximately calculated as 1.50 nm, in good agreement with that inferred from the TEM analysis carried out by Jeong et al. (1.45 nm) [19,20].

The Si/Ti ratio was measured by ICP and EDX. As shown in Table 1, the values obtained with both techniques were similar. By increasing the synthesis time, the Si/Ti ratio increased. In the case of the samples with a synthesis time of 24 h and 48 h, this ratio reached a value close to 5.5 which corresponds to the theoretical value of ETS-10.

3.2. Catalyst characterization

ETS-10 synthesized during 24 h at 230 °C was selected as support for Ru catalysts, despite the presence of residual TiO$_2$, because it presented a low content of ETS-4 impurities, the largest surface area and pore volume, and the Si/Ti ratio was close to the theoretical one for ETS-10.

Table 2
Intensity ratios for ETS-10 and Ru/ETS-10 measured by ICP.

Solids	Si/Ti	Na/Ti	K/Ti	Ru/Ti	Ru contents ICP (%)
ETS-10 24 h	4.10	1.55	0.57	–	–
RuH	4.03	1.74	0.57	0.014	0.6
RuG	4.32	1.86	0.81	–	0.5
RuI-DS	3.96	1.48	0.48	0.026	1.0
RuI-CS	4.20	1.25	0.67	0.115	4.2

Three strategies were followed to incorporate the ruthenium: in situ Ru load, incipient wetness impregnation and cation exchange. Table 2 summarizes the catalyst compositions measured by ICP. The Ru loading around to 0.6 wt.% was selected taking into account our previous work on Ru supported on lanthanum based oxides [6,7]. In the case of the exchanged samples, two different solution concentrations were employed producing catalysts with 1 and 4.2 wt.% of Ru from dilute and concentrated solutions, respectively.XRD patterns of the fresh (uncalcined) Ru catalysts are shown in Fig. 4. The signals coincide with the pattern of the titanosilicate structure. Note that the signal at 25.2° attributed to TiO$_2$, is lower in the RuG catalyst than in the other solids and the ETS-4 peak at 31° is better defined. In order to analyze whether the Ru incorporated in the synthesis gel has been substituted for Si^{4+} thus expanding the unit cell of ETS-10, the XRD pattern was zoomed and the peak shifts were investigated (Fig. 5). Howe and co-workers [21] observed in CoETS-10 catalysts a marked shift to lower angle in all diffraction peaks (e.g. by 0.25 for the 24.63° 2θ peak). The unit cell parameters calculated from the diffraction patterns (tetragonal unit cell) were: ETS-10, $a = 14.85$ Å, $c = 27.07$ Å; CoETS-10, $a = 15.11$ Å, $c = 27.79$ Å. Expansion of the unit cell is commonly seen when aluminum substitutes for silicon in alumino-silicate zeolites. Anderson et al. described similar (though smaller) expansions to those seen with CoETS-10 when Al^{3+} or Ga^{3+} are substituted by silicon in ETS-10 [22]. The respective ionic radii of Si^{4+} (40 pm), Al^{3+} (53 pm), Ga^{3+} (61 pm) and Co^{2+} (72 pm) are consistent with the observed magnitudes of the unit cell expansions at different loading levels of the substituting ions. In our case, according to the ionic radii of Ru (69 pm) the expected shift should be in the order of CoETS-10. However, ruthenium loading is considerably lower compared to the CoO in CoETS-10; therefore, it could be possible that the shift is not detectable by XRD and that part of the ruthenium was substituted in the structure of ETS-10.

Diffuse reflectance UV–vis spectra of ETS-10 and Ru/ETS-10 samples are shown in Fig. 6. The pure ETS-10 sample exhibits absorption only in the UV region, showing three major bands centered at 222, 263 and 294 nm. The band centered at 222 nm is due to

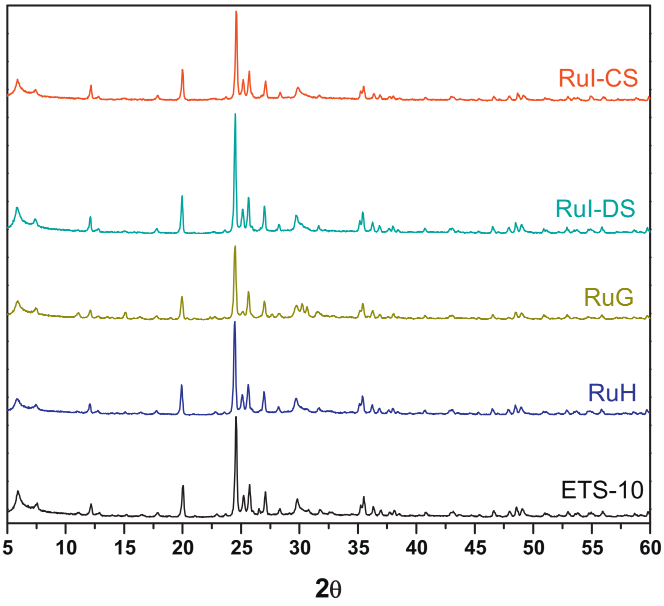

Fig. 4. XRD patterns of ETS-10 and Ru/ETS-10.

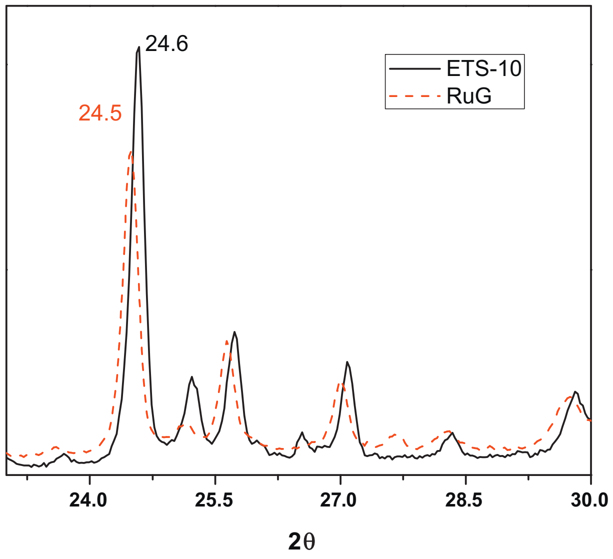

Fig. 5. Enlarged XRD patterns of ETS-10 and RuG (23–30° region).

the charge transfer from the Si and Ti-linking oxygen atoms to the Ti (IV) center atoms in directions perpendicular to the Ti—O—Ti—O chains [23]. The 263 and 294 nm bands are attributed to the charge transfer within the Ti—O—Ti—O chains of the ETS-10 structure [23]. The broad band around 330 nm in the prepared ETS-10 sample is due to TiO$_2$ phases [24], also detected by XRD.

A significant absorption can be observed in the visible range for the transition metal modified samples. According to the literature, the broad absorption bands in the range 400–800 nm could be ascribed to the presence of transition metals (Ni, Rh, and Pd) in the ETS-10 framework [25]. In this case the absorption in the visible range could be attributed to the presence of ruthenium. A significant absorption in the visible light region up to $\sim$650 nm was observed in the ETFeS-10 sample, although no distinct absorption band(s) could be distinguished in this energy range [26].

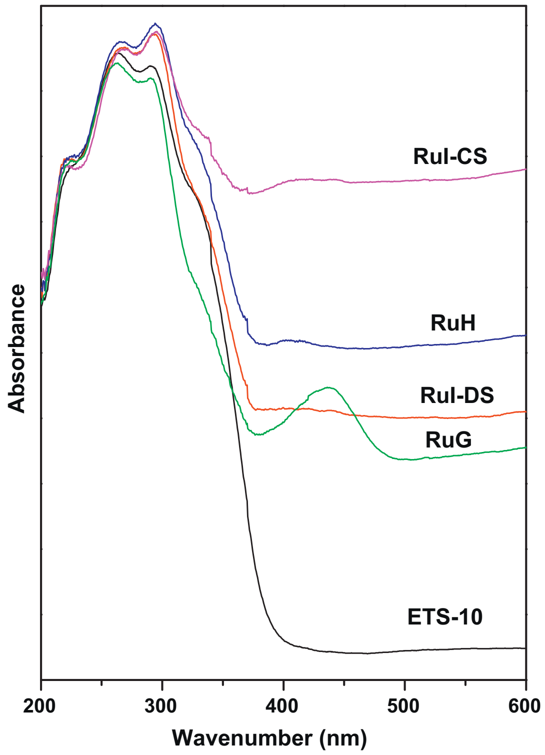

Fig. 6. UV–vis spectra of ETS-10 and Ru/ETS-10.

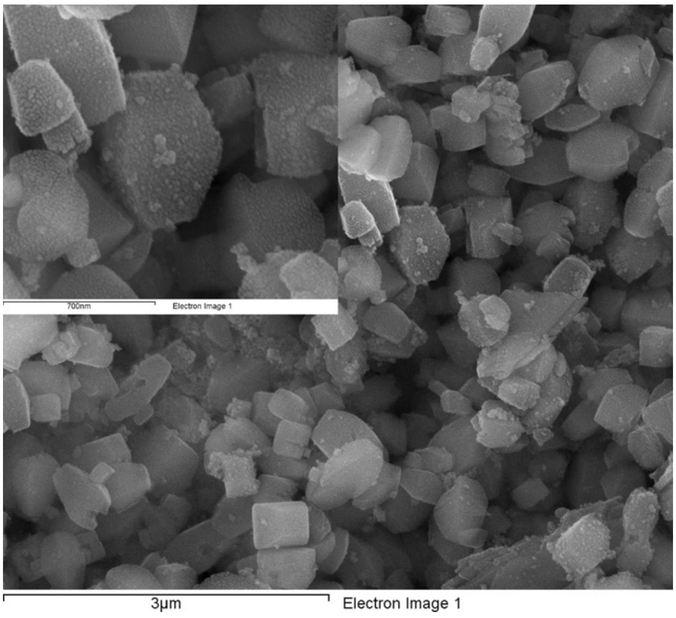

Fig. 7. SEM micrograph of reduced RuI-CS.

In ETCoS-10, the broad absorption bands observed at 390 nm and 500–700 nm have been assigned to tetrahedrally coordinated Co^{2+} that replaces Si^{4+} in the ETS-10 framework [27]. The authors claim that these UV–vis spectroscopic results, together with XRD analyses, suggest the incorporation of transition metal ions in the ETS-10 framework.

Liu and co-workers studied the electronic spectra of Ru complexes in the 800–200 nm range [28]. All the complexes show four to five intense absorptions in the 633–242 nm region. The intense absorptions in the 633–620 nm region are attributed to d–d transitions and the absorptions observed in the 430–413 nm region are probably due to charge transfer transitions (ligand to metal charge transfer) taking place from the filled ligand orbital (highest occupied molecular orbital) to the singly occupied ruthenium t$_2$ orbital. They concluded that the pattern of the electronic spectra of all the complexes indicated the presence of an octahedral environment around ruthenium(III) ion similar to that of other ruthenium(III) octahedral complexes [29].

In our solids, the UV–vis spectrum of RuG shows a different shape compared with the others catalysts. This sample exhibited an intense signal at 440 cm^{-1}, which would indicate that a ruthenium fraction might be substituted in the framework of ETS-10. This solid had the lower metal load (0.5% w/w) and this could be the reason why the changes were not observed in the positions of the XRD peaks (Table 2).

In the case of solids exchanged with dilute solutions (RuI-DS), the 440 cm^{-1} signal is not present suggesting that ruthenium would be located at exchange sites. In the case of RuI-CS solid with high Ru loading (4.2 wt.%), a low intensity band was observed suggesting that part of the ruthenium would be at exchange positions while another portion would form Ru oxides outside the titanosilicate structure.The SEM images for the RuI-CS catalyst show the presence of particles which are located on the surface of the ETS-10 crystals (Fig. 7). These particles were not observed in the SEM micrographs for RuG and RuH catalysts, probably due to the low concentration of ruthenium in these solids.However, the TEM micrographs showed the presence of nanoparticles on the truncated bipyramid of ETS-10 for RuH, RuG, RuI-DS and RuI-CS reduced catalysts (Fig. 8a–e). X-ray energy dispersive spectroscopy analysis confirmed that the

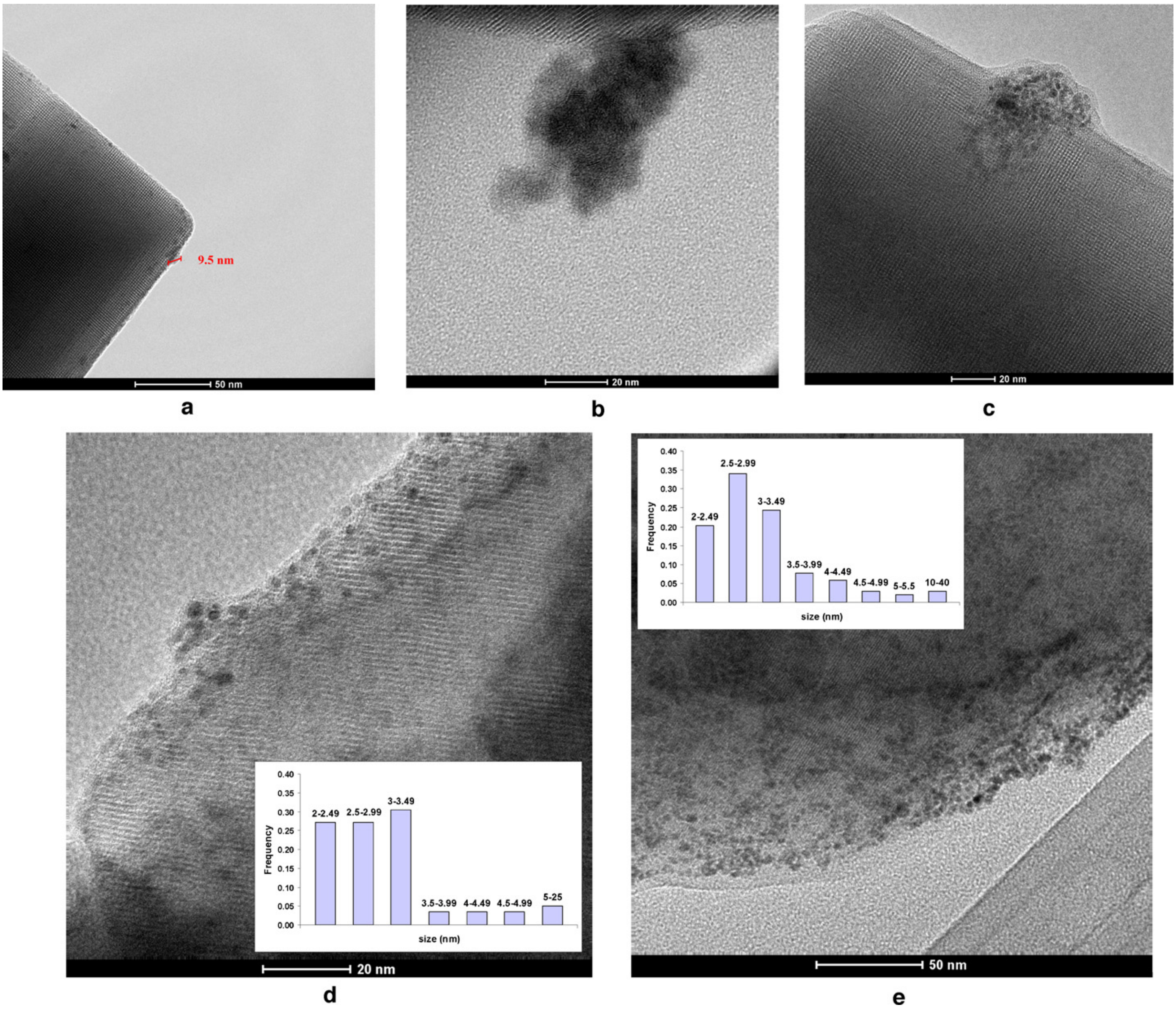

Fig. 8. TEM micrographs of reduced and oxidized solids (a) reduced RuH; (b) oxidized RuG; (c) reduced RuG; (d) reduced RuI-DS and (e) reduced RuI-CS.

observed particles contained ruthenium. It is also evident that the Ru nanoparticles are well dispersed in the RuH and RuI-DS catalysts. For the high Ru loading solid (RuI-CS), small Ru particles with sizes of 2–3 nm are uniformly distributed over the support. However, a low number of particles with sizes up to 40 nm were observed, leading to an average particle size of 6 nm. The histograms are included in Fig. 8d and e. The average size of Ru particles was calculated on the basis of size measurements of 250 particles for each sample. On the other hand, for the in situ Ru load sample (RuG) the TEM images before and after reduction show that the Ru particles are not uniformly distributed over the support, forming clusters (Fig. 8b and c).

Thermogravimetric analyses in N_2 flow were performed to study the thermal stability of the solids. All solids showed a mass loss of approximately 10% at temperatures below 300 °C due to the elimination of hydration H_2O present on the surface and inside the pores (Fig. 9). No other mass loss was observed up to 800 °C, in disagreement with Das et al. [30] that found a melting or phase transformation around 675 °C. This difference could be attributed to the use of templating agents [31]. Moreover, after reduction at

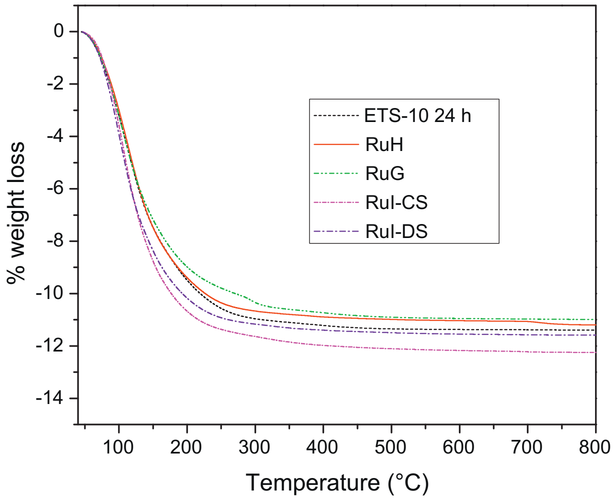

Fig. 9. Thermogravimetric analysis of ETS-10 and Ru/ETS-10.

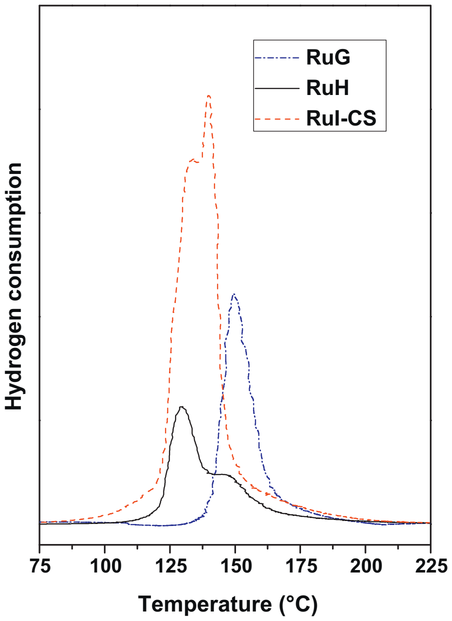

Fig. 10. TPR profiles of Ru solids after pretreatment in flowing N_2 at 300 °C.

550 °C in H_2 flow, the catalyst specific surface area showed a small variation of 10% in comparison with the calcined ETS-10.

A decrease in Langmuir surface area was previously reported [25] in the case of in situ transition metal loaded samples. The authors suggested that this could be due to the presence of impregnated transition metal cations in the pores of ETS-10 and to the loss of crystallinity during the metal loading. Note, that we do not observe this crystallinity decrease in our samples.

To study the reducibility of the Ru species present in the catalyst, temperature-programmed reduction studies were carried out for the uncalcined solids treated in situ under N_2 flow (Fig. 10). No reduction peaks were observed at temperatures between 225 °C and 550 °C for all samples. RuH and RuI-CS catalysts presented two main reduction peaks at 130 and 140 °C, while RuG showed only one signal at 150 °C even though no reduction peaks were detected for RuI-DS. In Ru/SiO_2 catalysts two reduction peaks at 150 and 200 °C were reported. The low temperature peak was assigned to well-dispersed RuO_x species and the high temperature to the reduction of RuO_2 particles [32]. The same assignments could be valid for the ETS-10 supported ruthenium species.

The higher reduction temperature for the RuG solid would be related to the larger size of the oxide particles. In this solid, a Ru fraction could be substituted in the ETS-10 framework (Fig. 6), while another portion could segregate on the titanosilicate particles (Fig. 8b).

From the hydrogen consumption results (not shown), the μmol H_2/μmol Ru ratios were calculated. For RuH catalyst, this ratio was close to 1.50, close to the Ru(III) oxide hydrogen consumption. Similar ratios were observed for our Ru catalysts supported on lanthanum based solids [6,7]. However, for the exchanged catalysts, this ratio was close to 2.5, suggesting the presence of more oxidized Ru species. Note, that the hydrogen consumption for the ETS-10 support was insignificant. On the other hand, the lack of reduction at temperatures lower than 550 °C could suggest that Ru is at exchange positions for the RuI-DS sample.

An XPS analysis was performed for qualitative and quantitative information on surface structure and composition of the ETS-10 and Ru/ETS-10 solids.

Before the XPS measurements, the solids were reduced in situ in the reaction chamber of the equipment at 400 °C in H_2 flux. Binding energies were referenced to C 1s = 284.6 eV, which resulted in a B.E. for Si 2s = 153.6 ± 0.2 eV for all the solids. There was an overlap between Ru 3d and C 1s peaks at 284.6 eV, the latter being due to carbonaceous contamination. The C 1s spectra also exhibited a peak at 287.8 eV that was attributed to carbonaceous species associated with oxygen and/or hydrogen. Ru 3d 5/2 core level exhibited two signals at about 279 and 281 eV, the low binding energy peak corresponding to Ru^0 and the other to Ru^{+n} (Table 3).

The binding energy of Ti $2p_{3/2}$ at 458.9 eV is characteristic of octahedrally coordinated Ti atoms in the —O—Ti—O—Ti—O— chains of ETS-10 [26]. This signal moved slightly towards higher energy in the exchanged samples. While several authors [32] observed no significant changes with different exchanged cations, such as Li^+, Na^+, K^+, Rb^+, Cs^+ and Ba^+, other authors reported increases in binding energies with the addition of Al, Bi and Fe in mesoporous titanosilicates [32].

The peak corresponding to O 1s (Table 3) can be decomposed into two contributions, the high intensity peak 531.9 eV attributed to O in the Si—O—Si and Si—O—Ti, and the lower intensity peak at 530.2 eV due to Ti—O—Ti [32].

Table 4 shows the XPS intensity ratio for the support and Ru solids. The surface Si/Ti ratio was higher in the case of the ETS-10 and RuG solid. However, for RuH and the exchanged samples (RuI-DS and RuI-CS) the values were close to 5 which is the theoretical value for the ETS-10 structure. The Na/Ti ratio was similar for the support and for RuH, whereas this value decreased in the case of exchanged samples and RuG. The surface Ru concentration was higher in the case of in situ load RuG solid. Note that this solid had the lowest Ru load. However, it presents the lowest dispersion and highest particle size as could be determined by CO chemisorption and confirmed by TEM results (Table 5). For the other solids, similar Ru/Ti XPS ratios were observed, despite their different Ru content, but similar average Ru particle sizes.

Bianchi and Ragaini [33] considered the Ru/Ti atomic ratio as a measure of the penetration of ruthenium inside the pores of the ETS-10 support modified by ion exchange with alkali metal ions. They observed that this ratio increases with increasing radius of the exchanged alkali metal. The Ru/Ti ratio becomes very high, because the active metal cannot penetrate the pores, due to the steric hindrance of the exchanged cesium cation.

Table 2 shows the ICP intensity ratio for the support and Ru solids. The Si/Ti was lower in the bulk than on the surface measured by XPS. For exchanged catalysts, the Na/Ti ratio decreases. However, in these solids the K/Ti ratio as well as the total cation to Ti ratio (i.e., Mt/Ti = (Na + K + Ru)/Ti) remained constant. Thus, in these Ru-ETS-10 samples Ru^{3+} ions gradually replaced Na^+ ions. A similar preference of Ag^+ ions to replace Na^+ ions was observed by Tiscornia and Ji [34,35]. The preferential exchange of Na^+ ions over K^+ ions can be explained by the locations of these cation types. The Na^+ ions are usually located at the 12-membered ring pores whereas K^+ ions prefer the less accessible 7-membered rings [36].

3.3. Catalytic activity for the dry reforming of methane

The catalytic activity was evaluated in a conventional fixed-bed reactor at 550 °C and the results are summarized in Table 5. The reaction rate values obtained for RuH and RuI catalysts are comparable to the Ru/zeolites reported in the literature and (Table 5), while for RuG no methane conversion was observed for the reaction under study. This behavior could be related to the presence of aggregates of ruthenium particles on the surface as was observed in the TEM images. Bueno and coworkers [5] used Y zeolites as support and found that these catalysts exhibited higher stability than those based on amorphous materials such as SiO_2 and Al_2O_3. In our catalyst, the highest reaction rate (mol g Ru h^{-1}) corresponded to the impregnated solid with well-dispersed Ru nanoparticles.

Table 3
Binding energies (eV) and signal percentages (%) of O 1s and Ru $3d_{5/2}$.

Solids	Ru incorporation	O 1s		Ru $3d_{5/2}$	
		Binding energy, eV (FWHM)	Signal percentage (%)	Binding energy, eV (FWHM)	Signal percentage (%)
ETS-10 24 h	–	531.9 (2.3)	76	–	–
		530.1 (2.1)	24		
RuH	Incipient	532.2 (2.2)	70	279.0 (1.8)	72
	Wetness impregnation	530.5 (2.2)	30	281.1 (2.2)	28
RuG	Synthesis gel	531.9 (2.3)	78	279.4 (2.2)	77
		530.2 (1.8)	22	281.4 (2.2)	23
RuI-DS	Ion exchanged	532.2 (2.2)	75	279.1 (1.9)	64
	[Ru] = 0.0015 M	530.5 (1.9)	25	281.1 (2.2)	36
RuI-CS	Ion exchanged	532.1 (2.3)	76	279.0 (1.9)	64
	[Ru] = 0.005 M	530.4 (1.9)	24	280.8 (2.2)	36

Table 4
Ruthenium contents of the catalysts measured by ICP and intensity ratios for ETS-10 and Ru/ETS-10 measured by XPS.

Solids	Ru contents ICP (%)	Ru/Ti ICP	Si/Ti	Na/Ti	K/Ti	Ru/Ti
ETS-10 24 h	–	–	6.1	1.9	0.66	–
RuH	0.6	0.014	4.7	1.9	0.58	0.28
RuG	0.5	–	6.2	1.4	1.47	0.81
RuI-DS	1.0	0.026	5.0	1.3	0.67	0.20
RuI-CS	4.2	0.115	5.2	1.5	0.85	0.26

A good agreement of the particle size calculation from CO chemisorption data and TEM results can be observed in Table 5. This table also shows that forward CH_4 turnover frequencies increased with increasing Ru dispersion, considering RuH and RuI-DS. This behavior is in agreement with what was reported by Wei and Iglesia [37,38] for Ru and other noble metals supported on non-carbonate forming oxides such as Al_2O_3 or ZrO_2 for CH_4—CO_2 and CH_4—H_2O reactions. For these catalysts, they showed that the reaction kinetics is first-order in methane and zero order in CO_2 partial pressures. For each metal, at least two supports were used to disperse metal clusters and no effects of support on turnover rates were detected. However, we have reported that there is no relationship between dispersion and TOF for carbonate forming oxides such us lanthanum based Rh and Ru catalysts [6,7,39]. The TOF values for our Ru lanhanum based catalysts are included for comparison.

Jones et al. [40] reported that the activity trend from their experimental work was as follows: Ru ~ Rh > Ni ~ Ir ~ Pt ~ Pd for CH_4—H_2O reactions with Ru TOF ranging between 2 and 20. They sustain that neither the detailed ranking nor the absolute activities agree with the work of Wei and Iglesia [37] where it was found that Pt is the most active steam reforming metal.

The stability tests for our Ru/ETS-10 catalysts are presented in Fig. 11. All solids (RuH, RuI-DS and RuI-CS) remained stable for more than 70 h in reaction. The CO_2 reaction rate (not shown) was higher than the CH_4 reaction rate due to the simultaneous occurrence of the reverse water gas shift (RWGS) reaction in which CO_2 reacted with the H_2 produced in the reforming reaction.

The XRD patterns show that the titanosilicate structure was stable after being exposed to the reaction mixture during 70 h at 550 °C (Fig. 12). Besides, the high Ru loading RuI-SC solid showed Ru sintering as could be observed in the XRD pattern measured after reaction. The particle size was calculated from this data. The particle size grows from 8 nm to 36 nm during reaction. However, no changes were observed in the catalyst activity during 70 h probably due to the high Ru loading providing enough active sites for the reaction. For this catalyst, the particle grown during reaction could lead to an erroneous TOF value calculated from the dispersion measured after reduction at 550 °C during 2 h (Table 5). Furthermore, for all the used catalysts, no carbon deposition was detected through Laser Raman spectroscopy, technique highly sensitive to graphitic carbon.

Table 5
Catalytic activity of Ru catalysts for the dry reforming of CH_4.

Catalyst	Ru load (%w/w)	r_{CH_4} (mol g Ru h^{-1})	D (%)[f]	dp [nm][g]	dp [nm][h]	TOF [s^{-1}]	H_2/CO
RuH[a]	0.6	40.0	9	10.0	8–10	12.5	0.29
RuG	0.5	–	3	30.0	20–30	–	–
RuI-DS[a]	1.0	6.0	5	18.0	7.7	3.4	0.35
RuI-CS[a]	4.2	6.2	11	8.2	5.8	1.6	0.30
Ru/HY[b]	1.0	1.87	–	–	–	–	0.63
Ru/NaY[b]	1.0	2.44	–	–	–	–	0.60
Ru/γ-Al_2O_3[c]	1.6	94.9	55.5	1.6	–	4.8	–
Ru/γ-Al_2O_3[c]	0.64	92.6	51.0	1.8	–	5.1	–
Ru/La_2O_3[d]	0.6	35.0	7	12.9	–	14.0	0.24
Ru/La_2O_3(50)-SiO_2[e]	0.6	81.7	38	2.4	–	6.0	0.36

[a] Reactant gas mixture composition: 32% CH_4 v/v, 32% CO_2, 36% Ar; W/F = 4.3 × 10^{-6} g h ml^{-1}; P = 1 atm. T = 550 °C.

[b] Ref. [5]. Reaction conditions: 100 ml/min, $CH_4/CO_2/N_2$ (20/20/60), $P_{CH_4} = 200$ Torr. T = 500 °C.

[c] Ref. [38]. Reaction conditions: $P_{CH_4} = 20$ KPa. T = 600 °C.

[d] Ref. [6]. Reaction conditions: see (a).

[e] Ref. [7]. Reaction conditions: see (a).

[f] Dispersion measured from CO chemisorption.

[g] To calculate the Ru particle size, the following equation was applied $dp = \frac{6 \cdot \upsilon_m}{D \cdot a_m}$; where, D is the metal dispersion (the ratio of the number of metal atoms on the support surface to the total number of metal atoms in the bulk), υ_m is the volume occupied by a metal atom m in the bulk (υ_m is 13.65 × 10^{-3} nm^3 for Ru), and a_m is the surface area occupied by an exposed surface metal atom m (9.09 × 10^{-2} nm^2) [7].

[h] Average diameters of Ru particles determined by counting around 250 particles on the TEM images using the equation: $dp = \frac{\sum n_i d_i^3}{\sum n_i d_i^2}$; where n_i is the number of particle of diameter d_i.

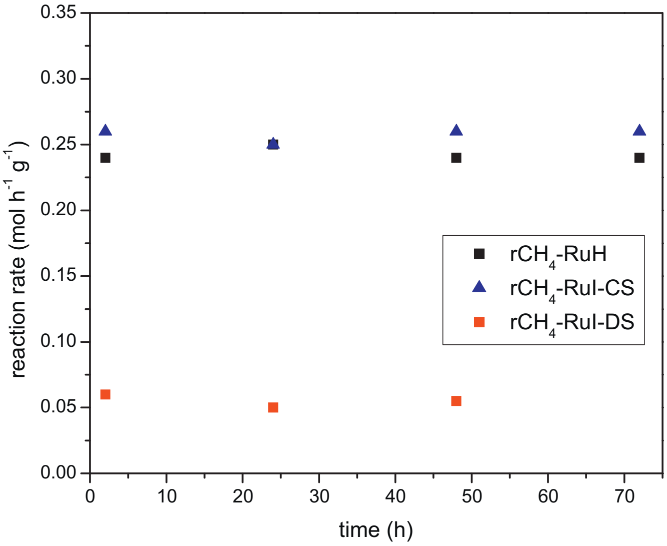

Fig. 11. Stability test of the catalysts after reduction at 550 °C in the fixed-bed reactor. (Reaction temperature = 550 °C, P = 1 atm, $W/F = 4.3 \times 10^{-6}$ g h ml^{-1}.) Feed composition: $P_{CH_4} : P_{CO_2} : P_{Ar} = 1 : 1 : 1.1$.

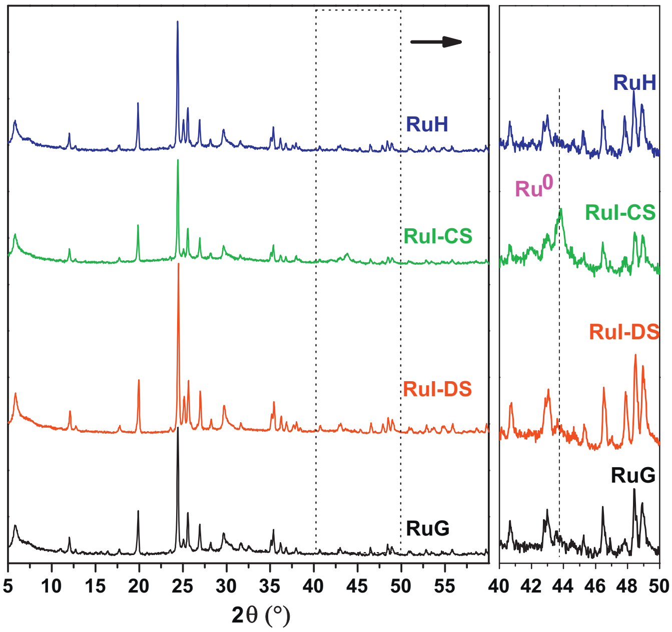

Fig. 12. XRD patterns of used RuG, RuH, RuI-CS and RuI-DS catalysts.

These results open an interesting line of research related to the optimization of operating conditions and application of these solids in other reactions producing hydrogen, such as the combined methane reforming.

4. Conclusions

High surface area microporous titanosilicates were synthesized to be applied as supports for ruthenium catalysts. When ruthenium was incorporated during the gel synthesis, a Ru fraction could be substituted in the ETS-10 framework, while another portion could segregate on the titanosilicate particles, and no catalytic activity was observed for the dry reforming of methane.

In addition, when the ETS-10 was exchanged with Ru concentrated solutions, part of the ruthenium would be at exchange positions while another portion would form Ru oxides outside the titanosilicate structure. The metallic Ru detected for this high loading RuI-CS catalyst indicates the sintering of Ru particles after being used during 50 h. This result is in agreement with its lowest turnover frequency value.

In the case of the solid exchanged with dilute solutions (RuI-DS), the lack of reduction at temperatures lower than 550 °C could suggest that Ru is at exchange positions, while for the incipient wetness impregnated catalyst (RuH) the Ru nano-particles were better dispersed. Therefore, RuH and RuI-DS catalysts were active and stable for the dry reforming of methane with the forward CH_4 turnover rates increasing with the increase in Ru dispersion. These results show the potential application of ETS-10 as support of Ru catalysts for H_2 production.

Acknowledgements

The authors wish to acknowledge the financial support received from UNL, CONICET and ANPCyT. Thanks are also given to the Japan International Cooperation Agency (JICA) for the donation of the XRD equipment, to ANPCyT for the purchase of the Raman instrument (PME 87-PAE 36985) and the UHV Multi Analysis System (PME 8-2003) and to Prof. Elsa Grimaldi for the English language editing. BF acknowledges CONICET's financial support during her stay at the University of Zaragoza.

References

[1] J. Rocha, M. Anderson, Eur. J. Inorg. Chem. 5 (2000) 801–818.
[2] M. Anderson, O. Terasaki, T. Oshuna, P. Malley, A. Philippou, S. MacKay, A. Ferreira, J. Rocha, S. Lidin, Philos. Mag. B 71 (1995) 813–841.
[3] A. Philippou, M. Naderi, N. Pervaiz, J. Rocha, M. Anderson, J. Catal. 178–1 (1998) 174–181.
[4] V. Sebastian, S. Irusta, R. Mallada, J. Santamaría, Appl. Catal. A: Gen. 366–2 (2009) 242–251.
[5] U.L. Portugal Jr., C.M.P. Marques, E.C.C. Araujo, E.V. Morales, M.V. Giotto, J.M.C. Bueno, Appl. Catal. A: Gen. 193 (2000) 173–183.
[6] B. Faroldi, C. Carrara, E.A. Lombardo, L. Cornaglia, Appl. Catal. A: Gen. 319 (2007) 38–46.
[7] B.M. Faroldi, E. Lombardo, L. Cornaglia, Appl. Catal. A: Gen. 369 (2009) 15–26.
[8] J. Rocha, A. Ferreira, Z. Lin, M. Anderson, Microporous Mesoporous Mater. 23 (1998) 253–263.
[9] X. Yang, J. Paillaud, H. van Breukelen, H. Kessler, E. Duprey, Microporous Mesoporous Mater. 46 (2001) 1–11.
[10] S. Uma, S. Rodrigues, I. Martyanov, K. Klabunde, Microporous Mesoporous Mater. 67 (2004) 181–187.
[11] A. Valente, Z. Lin, P. Brandao, I. Portugal, M. Anderson, J. Rocha, J. Catal. 200 (2001) 99–105.
[12] H. Li, B. Shen, X. Wang, S. Shen, Catal. Lett. 99 (2005) 165–169.
[13] Y. Goa, P. Wu, T. Tatsumi, J. Catal. 224 (2004) 107–114.
[14] S. Waghmode, V. Thakur, A. Sudalai, S. Sivasanker, Tetrahedron Lett. 42 (2001) 3145–3147.
[15] L. Lv, F. Su, X. Zhao, Microporous Mesoporous Mater. 76 (2004) 113–122.
[16] F.X.L.I. Xamena, P. Calza, C. Lamberti, C. Prestipino, A. Damin, S. Bordiga, E. Pelizzetti, A. Zecchina, J. Am. Chem. Soc. 125 (2003) 2264–2271.
[17] M.W. Anderson, J.R. Agger, N. Hanif, O. Terasaki, Microporous Mesoporous Mater. 48 (2001) 1–9.
[18] M.W. Anderson, J.R. Agger, N. Hanif, O. Terasaki, T. Ohsuna, Solid State Sci. 3 (2001) 809–819.
[19] N.C. Jeong, M.H. Lee, K.B. Yoon, Angew. Chem. Int. Ed. 46 (2007) 5868–5872.
[20] C. Casado, Z. Amghouz, J.R. García, K. Boulahya, J.M. González-Calbet, C. Téllez, J. Coronas, Mater. Res. Bull. 44 (2009) 1225–1231.
[21] A. Eldewik, R. Howe, Microporous Mesoporous Mater. 48 (2001) 65–71.
[22] M.W. Anderson, J. Rocha, Z. Lin, A. Phillipou, I. Orion, A. Ferreira, Microporous Mater. 6 (1996) 195–204.
[23] C. Lamberti, Microporous Mesoporous Mater. 30 (1999) 155–163.
[24] Z. Liu, R.J. Davis, J. Phys. Chem. 98 (1994) 1253–1261.
[25] K.P. Prasanth, H.C. Bajaj, H.D. Chung, K.Y. Choo, T.H. Kim, R.V. Jasra, Int. J. Hydrogen Energy 34 (2009) 888–896.
[26] Z. Ji, M.N. Ismail, D.M. Callahan Jr., J. Warzywoda, A. Sacco Jr., J. Photochem. Photobiol. A: Chem. 221 (2011) 77–83.
[27] A. Eldewik, R. Howe, Microporous Mater. 48 (2001) 65–71.
[28] S. Kannan, R. Ramesh, Y. Liu, J. Organomet. Chem. 692 (2007) 3380–3391.
[29] P.K. Sinha, J. Chakravarty, S. Bhattacharya, Polyhedron 16 (1997) 81–87.
[30] T. Das, A.J. Chandwadkar, A.P. Budhkar, S. Sivasanker, Microporous Mater. 5 (1996) 401–410.
[31] N.A. Turta, P. De Luca, N. Bilba, J.B. Nagy, A. Nastro, Microporous Mesoporous Mater. 112 (2008) 425–431.

[32] G. Yan, T. Wu, W. Weng, H. Toghiani, R.K. Toghiani, H.L. Wan, C.U. Pittman, J. Catal. 226 (2004) 247–259.

[33] C.L. Bianchi, V. Ragaini, J. Catal. 168 (1997) 70–74.

[34] I. Tiscornia, S. Irusta, P. Prádanos, C. Téllez, J. Coronas, J. Santamaría, J. Phys. Chem. C 111 (2007) 4702–4709.

[35] Z. Ji, M. Ismail, D. Callahan Jr., E. Pandowo, Z. Cai, T. Goodrich, K. Ziemer, J. Warzywoda, A. Sacco Jr., Appl. Catal. B: Environ. 102 (2011) 323–333.

[36] M.W. Anderson, J.R. Agger, D.-P. Luigi, A.K. Baggaley, J. Rocha, Phys. Chem. Chem. Phys. 1 (1999) 2287–2292.

[37] J.M. Wei, E. Iglesia, J. Phys. Chem. B 108 (2004) 4094–4103.

[38] J.M. Wei, E. Iglesia, J. Phys. Chem. B 108 (2004) 7253–7262.

[39] S. Irusta, J. Múnera, C. Carrara, E. Lombardo, L. Cornaglia, Appl. Catal. A: Gen. 287 (2005) 147–158.

[40] G. Jones, J. Jakobsen, S. Shim, J. Kleis, M. Andersson, J. Rossmeisl, F. Abild-Pedersen, T. Bligaard, S. Helveg, B. Hinnemann, J. Rostrup-Nielsen, I. Chorkendorff, J. Sehested, J. Nørskov, J. Catal. 259 (2008) 147–160.